Electronic Research Archive

https://www.aimspress.com/journal/era

ERA, 34(8): 5428–5451.
DOI: 10.3934/era.2026243
Received: 08 June 2026
Revised: 22 June 2026
Accepted: 23 June 2026
Published: 29 June 2026

Research article

Turing–Hopf bifurcation in a predator–prey model with cross-diffusion and herd behavior

Junci He, Dan Jin* and Ruizhi Yang

Department of Mathematics, Northeast Forestry University, Harbin 150040, China

* **Correspondence:** Email: jindan720@163.com.

Abstract: We studied a predator–prey reaction–diffusion system with cross-diffusion and a saturated herd-type functional response. The saturation effect introduces an extra ecological parameter that shifts both the Hopf and Turing–Hopf bifurcation thresholds away from those of the classical square-root model. The positive equilibrium was obtained in closed form, and linearization at this equilibrium yields characteristic equations for every spatial mode. Sharp conditions for local stability, Turing instability, and the codimension-two Turing–Hopf bifurcation were derived from these equations. A complete spectral description was provided so that the center spectrum at the bifurcation point consists of one pair of simple purely imaginary eigenvalues together with one simple zero eigenvalue. Using center manifold reduction and normal form theory for reaction–diffusion systems with cross-diffusion, we derived the third-order normal form on the center manifold. Numerical simulations verified the normal-form classification and displayed the stable spatially homogeneous and inhomogeneous steady states and periodic solutions that emerge near the bifurcation point.

Keywords: predator–prey model; herd behavior; cross-diffusion; Turing instability; Turing–Hopf bifurcation; normal form

1. Introduction

Predator–prey interaction is one of the most important mechanisms in population dynamics. Since the pioneering Lotka–Volterra models, many functional responses have been proposed to describe ecological interactions, including Holling type I, II, and III responses [1,2], ratio-dependent responses [3], Beddington–DeAngelis responses [4, 5], and responses with group defense or herd behavior. In natural ecosystems, prey may gather in herds to reduce predation risk. A common modeling approach is to assume that predators mainly attack individuals on the boundary of a herd. If the prey population occupies an area proportional to its density, then the number of individuals exposed to predation is proportional to the square root of the prey density. This mechanism leads to a square-root functional

response and was first introduced into predator–prey models by Rosenzweig and MacArthur [6]. Later, Ajraldi et al. [7] proposed a reaction–diffusion model with herd behavior, and Braza [8] studied the dynamics of the square-root response in the nondiffusive case. Tang and Song [9] further investigated cross-diffusion-induced spatiotemporal patterns in a predator–prey model with herd behavior.

Reaction–diffusion systems are used to describe the spatial movement of interacting species. Since Turing's seminal work [10] on the chemical basis of morphogenesis, diffusion-driven instability has become a central paradigm for understanding spatial pattern formation in biological, chemical, and ecological systems. Random dispersal of populations was first described mathematically by Skellam [11] and later summarized by Okubo and Levin [12]. A comprehensive review of pattern formation outside of equilibrium was given by Cross and Hohenberg [13]. In ecological contexts, reaction–diffusion models have successfully explained a wide range of spatial patterns, such as skin pigmentation, vegetation stripes, and plankton distributions [14]. In addition to self-diffusion, cross-diffusion is biologically meaningful because the density gradient of one species can influence the movement of another. Shigesada et al. [15] first introduced cross-diffusion terms to model the spatial segregation of interacting species. The effect of cross-diffusion on pattern formation and stability has been analyzed extensively by Lou and Ni [16] and has become an active topic in mathematical ecology [17–21].

Cross-diffusion is known to induce spatial pattern formation and Turing instability. Recent years have witnessed further developments in this direction. Song and Tang [22] investigated steady-state bifurcations and Turing patterns in a herd-behavior model with prey-taxis, showing that directed predator movement can significantly enlarge the parameter region of pattern formation. Peng and Yu [23] studied Turing patterns in a diffusive herd-behavior model with nonlocal delay, demonstrating that memory effects can induce novel spatiotemporal dynamics. Lv [24] analyzed Turing–Hopf bifurcation in a cross-diffusion predator–prey model with prey behavior transition, revealing how different prey defensive strategies affect bifurcation thresholds. These studies indicate that combining herd behavior with additional biological mechanisms (taxis, delay, nonlocality) continues to produce mathematically interesting and ecologically relevant results. The present paper contributes to this literature by introducing saturation in the herd-type functional response and analyzing its effect on the Turing–Hopf bifurcation.

For predator–prey systems with herd behavior, Turing–Hopf bifurcation is especially important, because it combines a spatially nonhomogeneous steady-state bifurcation and a temporal oscillatory bifurcation. The interaction between Turing and Hopf modes can generate rich spatiotemporal dynamics, including spatially homogeneous and inhomogeneous periodic solutions. The normal form theory for reaction–diffusion systems undergoing Turing–Hopf bifurcation was developed by Song et al. [25] and has been applied to various biological models [26]. The classical tools for Hopf bifurcation analysis, such as the center manifold theorem and normal form reduction, are well documented in Hassard et al. [27], Guckenheimer and Holmes [28], and Kuznetsov [29]. For partial differential equations with delays, Faria [30] established the normal form theory on center manifolds, and Wu [31] gave a systematic treatment of functional differential equations and their applications to reaction–diffusion systems.

Tang et al. [26] studied the Turing–Hopf bifurcation of a predator–prey model with herd behavior and cross-diffusion. Their model has the square-root response $\sqrt{u}v$. In the present paper, we consider a modified herd-behavior model with the saturated response

$$\frac{\sqrt{u}v}{1+a\sqrt{u}},$$

where $a > 0$ measures the saturation effect in predation. This additional parameter changes the location

of Hopf and Turing–Hopf bifurcation curves and leads to a different set of stability conditions. The main purpose of this paper is to derive the Turing instability and Turing–Hopf bifurcation conditions for this saturated herd-behavior model and to compute the corresponding normal form.

It is worth clarifying the relation between the present model and the classical square-root herd model studied in [26]. We discuss this comparison from three perspectives: the limit $a \to 0$, the structural change of bifurcation conditions, and the emergence of new dynamical regimes.

(i) The limit $a \to 0$. Setting $a = 0$ in the saturated response $\frac{\sqrt{u}v}{1+a\sqrt{u}}$ formally reduces it to $\sqrt{u}v$, which coincides with the functional response used in [26]. Consequently, the positive equilibrium (2.8) converges to $u^* \to s^2$ and $v^* \to s(1-s^2)$, recovering the equilibrium of the square-root model. However, the bifurcation structure does not degenerate in a smooth manner. In particular, the Hopf condition $J_{11} = 0$ becomes a cubic equation $f(a) = 0$ in the saturation parameter, rather than a fixed mortality relation. Moreover, the Turing–Hopf point is determined by the transversal intersection of the curves $a = a^*$ and $c = c_{k^*}(a)$ instead of a single point in the (s, c)-plane. This indicates that the saturated model cannot be interpreted as a straightforward perturbation of the square-root model.

(ii) Asymptotic behavior and saturation. For large prey density $u \gg 1$, the saturated response satisfies

$$\frac{\sqrt{u}v}{1 + a\sqrt{u}} \sim \frac{v}{a},$$

so the per-capita predation rate approaches the finite level $1/a$. In contrast, the classical square-root response $\sqrt{u}v$ grows unboundedly as $u \to \infty$. This saturation reflects the finite handling capacity of predators when prey density is high. The parameter a measures the inverse of this effective predation ceiling; larger a corresponds to stronger saturation and a lower ceiling.

(iii) New dynamical regimes and parameter-dependent differences. The saturation parameter introduces a new existence threshold $a < 1/s - 1$ (see (2.7)), which has no counterpart in the square-root model. As a approaches this threshold, the equilibrium satisfies $u^* \to +\infty$ and $v^* \to 0$ (see Remark 2.3), indicating a loss of predator persistence in the model. From the viewpoint of pattern formation, the normal-form coefficients differ quantitatively from those in [26], leading to shifted stability boundaries in the (μ_1, μ_2)-plane. In particular, for the parameter set in Section 5, both Hopf and Turing branches are supercritical ($\kappa_{11} < 0$, $\kappa_{22} < 0$), but the locations of the six dynamical regions and the coexistence ranges of multiple stable states differ from the classical square-root case. A detailed numerical comparison is provided in Section 5.

The rest of this paper is organized as follows. In Section 2, the model and its equilibria are given. In Section 3, the stability, Turing instability, and Turing–Hopf bifurcation are analyzed. In Section 4, the normal form on the center manifold is computed. In Section 5, numerical simulations are performed to illustrate the theoretical results. Conclusions are presented in Section 6.

2. Model formulation and equilibria

2.1. The model

We begin with the nondimensional predator–prey system

$$\begin{cases} \dfrac{\mathrm{d}u}{\mathrm{d}t} = u(1-u) - \dfrac{\sqrt{u}\,v}{1+a\sqrt{u}}, \\ \dfrac{\mathrm{d}v}{\mathrm{d}t} = cv\left(\dfrac{\sqrt{u}}{1+a\sqrt{u}} - s\right), \end{cases} \tag{2.1}$$

where $u(t)$ and $v(t)$ denote the densities of prey and predator, respectively. The parameter $a > 0$ measures the saturation intensity of the herd-type functional response, $s > 0$ is related to the predator mortality rate, and $c > 0$ is the conversion rate. The term $\sqrt{u}$ reflects the geometric fact that, when prey form a herd whose area is proportional to its density, only the individuals on the boundary are exposed to predation. The factor $1/(1 + a\sqrt{u})$ introduces saturation: as the prey density increases, the per capita predation rate eventually saturates rather than growing without bound.

To incorporate spatial dispersal, we consider the reaction–diffusion system

$$\begin{cases} \dfrac{\partial u}{\partial t} = d_{11}\Delta u + d_{12}\Delta v + u(1-u) - \dfrac{\sqrt{u}\,v}{1+a\sqrt{u}}, & x \in \Omega,\ t > 0, \\ \dfrac{\partial v}{\partial t} = d_{21}\Delta u + d_{22}\Delta v + cv\left(\dfrac{\sqrt{u}}{1+a\sqrt{u}} - s\right), & x \in \Omega,\ t > 0, \\ \dfrac{\partial u}{\partial \nu} = \dfrac{\partial v}{\partial \nu} = 0, & x \in \partial\Omega,\ t > 0, \\ u(x,0) = u_0(x) \geq 0, \quad v(x,0) = v_0(x) \geq 0, & x \in \Omega, \end{cases} \tag{2.2}$$

where $\Omega = (0, \ell\pi)$ and ν denotes the outward unit normal on the boundary $\partial\Omega$. The coefficients d_{11} and d_{22} are the self-diffusion rates, while d_{12} and d_{21} are the cross-diffusion coefficients. Throughout the paper, we assume

$$d_{11} > 0, \qquad d_{22} > 0, \qquad d_{11}d_{22} - d_{12}d_{21} > 0. \tag{2.3}$$

This guarantees that the diffusion matrix

$$D = \begin{pmatrix} d_{11} & d_{12} \\ d_{21} & d_{22} \end{pmatrix}$$

is normally elliptic in the one-dimensional setting considered here. The cross-diffusion coefficients may be positive or negative as long as (2.3) holds.

Remark 2.1. *The reaction term contains $\sqrt{u}$, so the vector field is not differentiable at $u = 0$. All local bifurcation analysis below is performed in a neighborhood of the positive equilibrium, where $u > 0$; hence the nonlinearity is smooth in the relevant region.*

Biologically, the cross-diffusion coefficients d_{12} and d_{21} describe directed movement of one species in response to the density gradient of the other. For example, $d_{21} > 0$ means predators chase the prey gradient (prey-taxis), while $d_{12} < 0$ may reflect prey avoidance of predator aggregation. The parabolicity

condition (2.3) ensures that the total flux $-D\nabla U$ is dissipative in the normally elliptic sense, which guarantees the well-posedness of the initial-boundary-value problem. In the one-dimensional setting considered here, this condition is satisfied for a wide range of biologically realistic cross-diffusion strengths, including cases where d_{12} and d_{21} have opposite signs.

2.2. Equilibria

The equilibria of (2.2) are determined by

$$\begin{cases} u(1-u) - \dfrac{\sqrt{u}\,v}{1+a\sqrt{u}} = 0, \\ cv\left(\dfrac{\sqrt{u}}{1+a\sqrt{u}} - s\right) = 0. \end{cases} \tag{2.4}$$

Clearly, $(0,0)$ and $(1,0)$ are boundary equilibria. A positive equilibrium (u^*, v^*) requires $u^* > 0$, $v^* > 0$, and

$$\frac{\sqrt{u^*}}{1+a\sqrt{u^*}} = s. \tag{2.5}$$

Solving (2.5) gives

$$\sqrt{u^*} = \frac{s}{1-as}, \qquad \text{hence} \qquad u^* = \frac{s^2}{(1-as)^2}. \tag{2.6}$$

For u^* to be positive and finite, we need $1-as > 0$, i.e., $a < 1/s$. Substituting (2.6) into the first equation of (2.4) yields

$$v^* = \frac{u^*(1-u^*)}{s} = \frac{s[(1-as)^2 - s^2]}{(1-as)^4}.$$

The positivity of v^* imposes the sharper condition $(1-as)^2 > s^2$, which, together with $1-as > 0$, is equivalent to

$$0 < a < \frac{1}{s} - 1. \tag{2.7}$$

Note that the admissible interval $(0, 1/s - 1)$ in (2.7) is nonempty only when $s < 1$, which is implicitly required for the existence of a positive equilibrium. Consequently, the positive equilibrium is given explicitly by

$$u^* = \frac{s^2}{(1-as)^2}, \qquad v^* = \frac{s[(1-as)^2 - s^2]}{(1-as)^4}. \tag{2.8}$$

Lemma 2.2. *System* (2.2) *has two boundary equilibria* $(0,0)$ *and* $(1,0)$. *If* (2.7) *holds, then* (2.2) *possesses a unique positive equilibrium* (u^*, v^*) *given by* (2.8).

Remark 2.3. *The explicit Eq* (2.8) *allows direct asymptotic analysis.*

(i) ***Small saturation*** *($a \to 0^+$). One recovers the square-root model equilibrium $u^* \sim s^2$, $v^* \sim s(1-s^2)$. In this limit, the predation rate grows unboundedly with prey density, and the bifurcation structure reduces to that studied in [26].*

(ii) ***Large predator mortality*** *($s \to 1^-$) **with fixed*** *a. Both u^* and v^* tend to zero because the prey herd collapses and the predator starves. This is the biologically relevant limit: high mortality*

suppresses predation pressure, allowing prey to approach its carrying capacity $u = 1$, but the equilibrium condition (2.5) *forces $u^* \to 0$ as $s \to 1^-$ because the predation rate at the boundary cannot match the high mortality demand.*

(iii) ***Approaching the existence boundary*** *($a \to (1/s - 1)^-$). The equilibrium density $u^* = s^2/(1 - as)^2$ diverges to $+\infty$ while $v^* \to 0$. This divergence is a structural feature of the saturated model: when the saturation parameter a is too large, the functional response becomes so flat that the predator cannot sustain a positive population, and the prey density explodes toward its carrying capacity. In the square-root model ($a = 0$), this collapse does not occur because the predation rate grows without bound, always allowing a predator–prey coexistence equilibrium for any $s \in (0, 1)$.*

(iv) ***Small s with fixed a.*** *The equilibrium satisfies $u^* \sim s^2$ and $v^* \sim s$, so the prey density is small but the predator density scales linearly with s. These scalings are useful for interpreting the bifurcation thresholds in limiting parameter regimes.*

3. Linear stability and bifurcation analysis

3.1. Linearization and characteristic equations

Let $U = (u, v)^{\mathrm{T}}$. Linearizing (2.2) at the positive equilibrium (u^*, v^*) gives

$$\frac{\partial U}{\partial t} = D\Delta U + JU, \tag{3.1}$$

where the Jacobian matrix is

$$J = \begin{pmatrix} J_{11} & J_{12} \\ J_{21} & J_{22} \end{pmatrix} = \begin{pmatrix} 1 - 2u^* - \dfrac{s(1-u^*)}{2\sqrt{u^*}} & -s \\ \dfrac{cs(1-u^*)}{2\sqrt{u^*}} & 0 \end{pmatrix}. \tag{3.2}$$

It is convenient to write

$$J_{11} = \frac{f(a)}{2(1-as)^2}, \qquad J_{21} = cJ(a),$$

with

$$f(a) = a^3s^3 - a^2s^2 - a(s^3 + s) - 3s^2 + 1, \qquad J(a) = \frac{a^2s^2 - 2as - s^2 + 1}{2(1-as)}.$$

Under (2.7), one has $J(a) > 0$, and hence $J_{21} > 0$ for every $c > 0$.

Consider the Neumann eigenvalue problem on $\Omega = (0, \ell\pi)$:

$$-\vartheta'' = \mu\vartheta, \quad x \in (0, \ell\pi), \quad \vartheta'(0) = \vartheta'(\ell\pi) = 0.$$

Its eigenvalues are $\mu_k = k^2/\ell^2$ ($k = 0, 1, 2, \dots$) with eigenfunctions proportional to $\cos(kx/\ell)$. For the kth spatial mode, the characteristic matrix is

$$M_k = \begin{pmatrix} J_{11} - d_{11}\mu_k & J_{12} - d_{12}\mu_k \\ J_{21} - d_{21}\mu_k & J_{22} - d_{22}\mu_k \end{pmatrix},$$

and the associated characteristic equation reads

$$\lambda^2 - T_k\lambda + D_k = 0, \qquad k \in \mathbb{N}_0, \tag{3.3}$$

where

$$T_k = J_{11} - (d_{11} + d_{22})\mu_k, \tag{3.4}$$

$$D_k = (d_{11}d_{22} - d_{12}d_{21})\mu_k^2 - (d_{21}s + d_{22}J_{11} - d_{12}J_{21})\mu_k + sJ_{21}. \tag{3.5}$$

Consequently, the positive equilibrium is locally asymptotically stable if and only if

$$T_k < 0, \qquad D_k > 0, \qquad k = 0, 1, 2, \ldots. \tag{3.6}$$

3.2. ODE stability and Hopf bifurcation

For the ODE system without diffusion ($k = 0$), Eq (3.3) reduces to

$$\lambda^2 - J_{11}\lambda + sJ_{21} = 0. \tag{3.7}$$

Since $J_{21} > 0$, the equilibrium is stable exactly when

$$J_{11} < 0. \tag{3.8}$$

The Hopf bifurcation threshold is determined by $J_{11} = 0$, i.e.,

$$f(a) = 0. \tag{3.9}$$

Let a^* be a simple root of (3.9) in the admissible interval $(0, 1/s - 1)$:

$$f(a^*) = 0, \qquad f'(a^*) \neq 0. \tag{3.10}$$

At $a = a^*$, the characteristic roots of (3.7) are $\lambda = \pm i\omega_c$ with

$$\omega_c = \sqrt{sJ_{21}(a^*, c)} > 0. \tag{3.11}$$

Moreover,

$$\left.\frac{\mathrm{d}\,\mathrm{Re}\,\lambda}{\mathrm{d}a}\right|_{a=a^*} = \frac{f'(a^*)}{4(1 - a^*s)^2} \neq 0, \tag{3.12}$$

so the Hopf crossing is transversal.

Theorem 3.1. *Assume* (2.7) *and* $J_{11} < 0$*. Then the positive equilibrium* (u^*, v^*) *of the ODE system* (2.1) *is locally asymptotically stable. If* $a = a^*$ *satisfies* (3.10)*, then the ODE system undergoes a Hopf bifurcation at* (u^*, v^*)*.*

Proof. For the ODE system, the characteristic equation is (3.7). Since $sJ_{21} > 0$, the Routh–Hurwitz criterion gives stability when $J_{11} < 0$. At $a = a^*$, we have $J_{11} = 0$ and the roots are $\pm i\omega_c$. Transversality follows from (3.12). □

If $d_{12} = d_{21} = 0$, then

$$D_k = d_{11}d_{22}\mu_k^2 - d_{22}J_{11}\mu_k + sJ_{21} > 0$$

whenever $J_{11} < 0$. Hence self-diffusion alone cannot induce Turing instability in the present model.

Theorem 3.2. *Assume* $d_{12} = d_{21} = 0$*,* $d_{11} > 0$*,* $d_{22} > 0$*, and* $J_{11} < 0$*. Then the positive equilibrium of* (2.2) *is locally asymptotically stable.*

Proof. For all $k \geq 0$, $T_k = J_{11} - (d_{11} + d_{22})\mu_k < 0$. Moreover, $D_k = d_{11}d_{22}\mu_k^2 - d_{22}J_{11}\mu_k + sJ_{21} > 0$. Therefore (3.6) holds for every spatial mode. □

3.3. Turing instability induced by cross-diffusion

Let

$$A = d_{11}d_{22} - d_{12}d_{21} > 0, \qquad B = d_{21}s + d_{22}J_{11} - d_{12}J_{21}. \tag{3.13}$$

Then D_k can be rewritten as

$$D(\mu_k) = A\mu_k^2 - B\mu_k + sJ_{21}. \tag{3.14}$$

If $B \le 0$, then $D(\mu) > 0$ for all $\mu \ge 0$. If $B > 0$, Turing instability is possible only when the discriminant

$$\Delta_T = B^2 - 4AsJ_{21} > 0. \tag{3.15}$$

In that case, setting

$$z_\pm = \frac{B \pm \sqrt{\Delta_T}}{2A}, \tag{3.16}$$

we have $D(\mu) < 0$ for $\mu \in (z_-, z_+)$. Thus the positive equilibrium is Turing unstable if there exists $k \in \mathbb{N}$ such that $\mu_k \in (z_-, z_+)$, while the corresponding ODE equilibrium is stable.

Theorem 3.3. *Assume* (2.7), (2.3), $J_{11} < 0$, *and* $J_{21} > 0$. *Then the following assertions hold:*

(i) If $B \le 0$, the positive equilibrium is locally asymptotically stable.

(ii) If $B > 0$ and $\Delta_T < 0$, the positive equilibrium is locally asymptotically stable.

(iii) If $B > 0$, $\Delta_T > 0$, and there exists $k^* \in \mathbb{N}$ such that $\mu_{k^*} \in (z_-, z_+)$, then the positive equilibrium is Turing unstable.

Proof. Since $J_{11} < 0$, we have $T_k < 0$ for all $k \ge 0$. Thus stability is determined solely by the sign of $D_k = D(\mu_k)$. The three conclusions follow directly from the quadratic function (3.14). □

3.4. Turing–Hopf bifurcation

A Turing–Hopf bifurcation occurs when the homogeneous mode $k = 0$ has a pair of simple purely imaginary eigenvalues and one non-zero spatial mode k^* has a simple zero eigenvalue, while all remaining eigenvalues have negative real parts.

For $a = a^*$, $J_{11} = 0$ and the Hopf condition is satisfied. The Turing condition $D_k = 0$ for mode k yields

$$c_k(a) = \frac{[d_{21}s + d_{22}J_{11}(a) - A\mu_k]\mu_k}{(d_{12}\mu_k + s)J(a)}, \qquad k \in \mathbb{N}. \tag{3.17}$$

A positive value $c_k(a^*)$ is possible only if

$$k \in S := \left\{ k \in \mathbb{N} : \ \mu_k < \frac{d_{21}s}{A} \right\}. \tag{3.18}$$

Suppose $S \neq \emptyset$ and choose $k^* \in S$ such that

$$c^* = c_{k^*}(a^*) > 0, \qquad c_{k^*}(a^*) \neq c_k(a^*) \quad \text{for all } k \in S,\ k \neq k^*. \tag{3.19}$$

The uniqueness condition (3.19) excludes multiple Turing critical modes.

Hypothesis 3.4. *At $(a, c) = (a^*, c^*)$, the following spectral conditions hold:*

(H1) $f(a^*) = 0$ *and* $f'(a^*) \neq 0$*;*

(H2) $D_{k^*}(a^*, c^*) = 0$ *and* $T_{k^*}(a^*, c^*) << 0$*;*

(H3) $D_k(a^*, c^*) > 0$ *for all* $k \neq k^*$, $k \geq 1$*;*

(H4) $c'_{k^*}(a^*) \neq 0$.

Remark 3.5. *In (H2), we write $T_{k^*}(a^*, c^*) << 0$ rather than $T_{k^*}(a^*, c^*) < 0$ to stress that the trace must be strictly negative and bounded away from zero at the bifurcation point. This guarantees that the zero eigenvalue of the Turing mode is simple and that no additional eigenvalues cross the imaginary axis along the trace direction, which is essential for the codimension-two unfolding.*

Theorem 3.6. *Assume* (2.7), (2.3)*, and Hypothesis 3.4. Then system* (2.2) *undergoes a codimension-two Turing–Hopf bifurcation at $(a, c) = (a^*, c^*)$. More precisely, the center spectrum consists of*

$$\Lambda_c = \{\mathrm{i}\omega_c, -\mathrm{i}\omega_c, 0\},$$

where $\pm\mathrm{i}\omega_c$ correspond to the homogeneous mode $k = 0$ and the zero eigenvalue corresponds to the nonhomogeneous mode $k = k^*$.

Proof. At $a = a^*$, $J_{11} = 0$ and the homogeneous characteristic equation has roots $\pm\mathrm{i}\omega_c$ with ω_c given by (3.11). Since $f'(a^*) \neq 0$, the Hopf crossing is transversal by (3.12). At $c = c_{k^*}(a^*)$, $D_{k^*} = 0$. Since $T_{k^*} << 0$, the zero root is simple. By Hypothesis 3.4(H3), all other modes are hyperbolic and stable. Finally, $c'_{k^*}(a^*) \neq 0$ implies that the Hopf curve and the Turing curve intersect transversally. Hence the bifurcation is of codimension two. □

4. Normal form on the center manifold

4.1. Preliminaries and linear coefficients

We choose the bifurcation parameters

$$a = a^* + \mu_1, \qquad c = c^* + \mu_2, \qquad \mu = (\mu_1, \mu_2) \in \mathbb{R}^2. \tag{4.1}$$

Throughout this section, the inner product for complex vectors is the standard Euclidean inner product $\langle p, q\rangle = q^{\mathrm{T}} p$ (transpose, not conjugate transpose), and the adjoint eigenvectors are normalized according to $q^{\mathrm{T}} p = 1$ as stated in (4.6) and (4.8). This convention follows the normal-form framework for reaction–diffusion systems with cross-diffusion developed in [25].

Since the positive equilibrium depends on a, we write

$$u^*(\mu_1) = \frac{s^2}{\left[1 - (a^* + \mu_1)s\right]^2}, \qquad v^*(\mu_1) = \frac{s\{\left[1 - (a^* + \mu_1)s\right]^2 - s^2\}}{\left[1 - (a^* + \mu_1)s\right]^4}. \tag{4.2}$$

Set $\bar{u} = u - u^*(\mu_1)$ and $\bar{v} = v - v^*(\mu_1)$, drop the bars, and denote $U = (u, v)^{\mathrm{T}}$. System (2.2) then becomes

$$\frac{\partial U}{\partial t} = D\Delta U + L_0 U + F(U, \mu), \tag{4.3}$$

where

$$L_0 U = \begin{pmatrix} J_{11}(a^*)u + J_{12}(a^*)v \\ J_{21}(a^*, c^*)u + J_{22}(a^*)v \end{pmatrix}. \tag{4.4}$$

Notice that $J_{12} = -s$ and $J_{22} = 0$. The nonlinear term is expanded as

$$F(U, \mu) = \sum_{i+j+l_1+l_2 \geq 2} \frac{1}{i!\, j!\, l_1!\, l_2!} f_{ijl_1l_2}\, u^i v^j \mu_1^{l_1} \mu_2^{l_2}, \tag{4.5}$$

with

$$f_{ijl_1l_2} = \begin{pmatrix} f^{(1)}_{ijl_1l_2} \\ f^{(2)}_{ijl_1l_2} \end{pmatrix}, \qquad f^{(m)}_{ijl_1l_2} = \left. \frac{\partial^{i+j+l_1+l_2} \widetilde{f}^{(m)}}{\partial u^i\, \partial v^j\, \partial \mu_1^{l_1}\, \partial \mu_2^{l_2}} \right|_{(0,0,0,0)},$$

and

$$\widetilde{f}^{(1)} = (u + u^*)[1 - u - u^*] - \frac{\sqrt{u + u^*}\,(v + v^*)}{1 + (a^* + \mu_1)\sqrt{u + u^*}},$$
$$\widetilde{f}^{(2)} = (c^* + \mu_2)(v + v^*)\left(\frac{\sqrt{u + u^*}}{1 + (a^* + \mu_1)\sqrt{u + u^*}} - s \right).$$

At the Turing–Hopf point, the critical subspace is spanned by the eigenvectors of M_0 and M_{k^*}. For the Hopf mode $k = 0$, we choose

$$p_0 = \begin{pmatrix} 1 \\ \dfrac{\mathrm{i}\omega_c}{J_{12}(a^*)} \end{pmatrix}, \qquad q_0 = \begin{pmatrix} \dfrac{1}{2} \\ \dfrac{J_{12}(a^*)}{2\mathrm{i}\omega_c} \end{pmatrix}, \tag{4.6}$$

normalized so that $q_0^{\mathrm{T}} p_0 = 1$. Since $J_{12} = -s$, this is equivalent to

$$p_0 = \begin{pmatrix} 1 \\ -\mathrm{i}\omega_c / s \end{pmatrix}, \qquad q_0 = \begin{pmatrix} 1/2 \\ \mathrm{i}s/(2\omega_c) \end{pmatrix}.$$

For the Turing mode $k = k^*$, we take

$$p_{k^*} = \begin{pmatrix} 1 \\ \dfrac{J_{21}(a^*, c^*) - d_{21}\mu_{k^*}}{d_{22}\mu_{k^*}} \end{pmatrix}, \tag{4.7}$$

and select the adjoint eigenvector q_{k^*} so that $q_{k^*}^{\mathrm{T}} p_{k^*} = 1$. A direct computation gives

$$q_{k^*} = \frac{1}{\Theta} \begin{pmatrix} d_{22}\mu_{k^*} \\ -(J_{12}(a^*) - d_{12}\mu_{k^*}) \end{pmatrix}, \tag{4.8}$$

where

$$\Theta = d_{22}\mu_{k^*} - (J_{12}(a^*) - d_{12}\mu_{k^*}) \frac{J_{21}(a^*, c^*) - d_{21}\mu_{k^*}}{d_{22}\mu_{k^*}}. \tag{4.9}$$

Following the normal-form procedure for reaction–diffusion systems with cross-diffusion, the third-order normal form on the center manifold is

$$\begin{cases} \dot{\rho} = \alpha_1(\mu)\rho + \kappa_{11}\rho^3 + \kappa_{12}\rho r^2 + O(|(\rho, r)|^5 + |\mu|\,|(\rho, r)|^3), \\ \dot{r} = \alpha_2(\mu)r + \kappa_{21}\rho^2 r + \kappa_{22}r^3 + O(|(\rho, r)|^5 + |\mu|\,|(\rho, r)|^3), \end{cases} \tag{4.10}$$

with

$$\alpha_1(\mu) = \mathrm{Re}(B_{11})\mu_1 + \mathrm{Re}(B_{21})\mu_2, \qquad \alpha_2(\mu) = B_{13}\mu_1 + B_{23}\mu_2, \tag{4.11}$$

and

$$\kappa_{11} = \mathrm{Re}(B_{210}), \quad \kappa_{12} = \mathrm{Re}(B_{102}), \quad \kappa_{21} = B_{111}, \quad \kappa_{22} = B_{003}. \tag{4.12}$$

The linear coefficients are

$$\begin{aligned} B_{11} &= p_{01}\, q_0^{\mathrm{T}} f_{1010} + p_{02}\, q_0^{\mathrm{T}} f_{0110}, \\ B_{21} &= p_{01}\, q_0^{\mathrm{T}} f_{1001} + p_{02}\, q_0^{\mathrm{T}} f_{0101}, \\ B_{13} &= p_{k^*1}\, q_{k^*}^{\mathrm{T}} f_{1010} + p_{k^*2}\, q_{k^*}^{\mathrm{T}} f_{0110}, \\ B_{23} &= p_{k^*1}\, q_{k^*}^{\mathrm{T}} f_{1001} + p_{k^*2}\, q_{k^*}^{\mathrm{T}} f_{0101}. \end{aligned} \tag{4.13}$$

4.2. Explicit third-order coefficients

The vectors F_{ijk} collect the quadratic and cubic terms of the Taylor expansion projected onto the critical eigenspaces; the coefficients h_{ijk} are the second-order corrections on the center manifold obtained by solving the homological equations; and B_{ijk} assemble the final cubic normal-form coefficients through the combination of direct cubic terms (C_{ijk}), second-order resonant corrections (D_{ijk}), and center-manifold interactions (E_{ijk}). The numerical evaluation proceeds by first computing the partial derivatives $f_{ijl_1l_2}$ at the bifurcation point, then constructing F_{ijk}, solving for h_{ijk}, and finally substituting into the B_{ijk} formulas.

For convenience, write $p_0 = (p_{01}, p_{02})^{\mathrm{T}}$ and $p_{k^*} = (p_{k^*1}, p_{k^*2})^{\mathrm{T}}$. Define the quadratic vectors

$$\begin{aligned} F_{200} &= p_{01}^2 f_{2000} + 2p_{01}p_{02} f_{1100} + p_{02}^2 f_{0200}, \\ F_{020} &= \overline{F}_{200}, \\ F_{002} &= p_{k^*1}^2 f_{2000} + 2p_{k^*1}p_{k^*2} f_{1100} + p_{k^*2}^2 f_{0200}, \\ F_{110} &= |p_{01}|^2 f_{2000} + 2\,\mathrm{Re}(p_{01}\overline{p}_{02}) f_{1100} + |p_{02}|^2 f_{0200}, \\ F_{101} &= p_{01}p_{k^*1} f_{2000} + (p_{01}p_{k^*2} + p_{02}p_{k^*1}) f_{1100} + p_{02}p_{k^*2} f_{0200}, \\ F_{011} &= \overline{F}_{101}, \end{aligned}$$

and the cubic vectors

$$\begin{aligned} F_{210} = \frac{1}{2}\Big[& f_{3000}|p_{01}|^2 p_{01} + f_{0300}|p_{02}|^2 p_{02} + f_{2100}(p_{01}^2\overline{p}_{02} + 2|p_{01}|^2 p_{02}) \\ & + f_{1200}(p_{02}^2\overline{p}_{01} + 2|p_{02}|^2 p_{01})\Big], \\ F_{102} = \frac{1}{2}\Big[& f_{3000}p_{k^*1}^2 p_{01} + f_{0300}p_{k^*2}^2 p_{02} + f_{2100}(p_{k^*1}^2 p_{02} + 2p_{01}p_{k^*1}p_{k^*2}) \\ & + f_{1200}(p_{k^*2}^2 p_{01} + 2p_{02}p_{k^*1}p_{k^*2})\Big], \end{aligned}$$

$$
\begin{aligned}
F_{111} &= f_{3000}|p_{01}|^2 p_{k^*1} + f_{0300}|p_{02}|^2 p_{k^*2} \\
&\quad + f_{2100}(|p_{01}|^2 p_{k^*2} + 2p_{k^*1}\,\mathrm{Re}(p_{01}\overline{p}_{02})) \\
&\quad + f_{1200}(|p_{02}|^2 p_{k^*1} + 2p_{k^*2}\,\mathrm{Re}(p_{02}\overline{p}_{01})), \\
F_{003} &= \frac{1}{6}(f_{3000}p_{k^*1}^3 + f_{0300}p_{k^*2}^3) + \frac{1}{2}(f_{2100}p_{k^*1}^2 p_{k^*2} + f_{1200}p_{k^*1}p_{k^*2}^2).
\end{aligned}
$$

The second-order center-manifold corrections are obtained from the homological equations:

$$
\begin{aligned}
h_{0200} &= \frac{1}{\sqrt{\ell\pi}}(2\mathrm{i}\omega_c I - M_0)^{-1}\{F_{200} - (q_0^{\mathrm{T}}F_{200})p_0 - (\overline{q}_0^{\mathrm{T}}F_{200})\overline{p}_0\}, \\
h_{0020} &= \frac{1}{\sqrt{\ell\pi}}(-2\mathrm{i}\omega_c I - M_0)^{-1}\{F_{020} - (q_0^{\mathrm{T}}F_{020})p_0 - (\overline{q}_0^{\mathrm{T}}F_{020})\overline{p}_0\}, \\
h_{0002} &= -\frac{1}{\sqrt{\ell\pi}}M_0^{-1}\{F_{002} - (q_0^{\mathrm{T}}F_{002})p_0 - (\overline{q}_0^{\mathrm{T}}F_{002})\overline{p}_0\}, \\
h_{0110} &= -\frac{2}{\sqrt{\ell\pi}}M_0^{-1}\{F_{110} - (q_0^{\mathrm{T}}F_{110})p_0 - (\overline{q}_0^{\mathrm{T}}F_{110})\overline{p}_0\}, \\
h_{k^*101} &= \frac{2}{\sqrt{\ell\pi}}(\mathrm{i}\omega_c I - M_{k^*})^{-1}\{F_{101} - (q_{k^*}^{\mathrm{T}}F_{101})p_{k^*}\}, \\
h_{k^*011} &= \frac{2}{\sqrt{\ell\pi}}(-\mathrm{i}\omega_c I - M_{k^*})^{-1}\{F_{011} - (q_{k^*}^{\mathrm{T}}F_{011})p_{k^*}\}, \\
h_{(2k^*)002} &= -\frac{1}{\sqrt{2\ell\pi}}M_{2k^*}^{-1}F_{002}, \qquad h_{(2k^*)110} = (0,0)^{\mathrm{T}}.
\end{aligned}
$$

The cubic normal-form coefficients are assembled as

$$
\begin{aligned}
B_{210} &= C_{210} + \frac{3}{2}(D_{210} + E_{210}), \\
B_{102} &= C_{102} + \frac{3}{2}(D_{102} + E_{102}), \\
B_{111} &= C_{111} + \frac{3}{2}(D_{111} + E_{111}), \\
B_{003} &= C_{003} + \frac{3}{2}(D_{003} + E_{003}),
\end{aligned}
$$

where

$$
\begin{aligned}
C_{210} &= \frac{1}{\ell\pi}q_0^{\mathrm{T}}F_{210}, & C_{102} &= \frac{1}{\ell\pi}q_0^{\mathrm{T}}F_{102}, \\
C_{111} &= \frac{1}{\ell\pi}q_{k^*}^{\mathrm{T}}F_{111}, & C_{003} &= \frac{3}{2\ell\pi}q_{k^*}^{\mathrm{T}}F_{003},
\end{aligned}
$$

$$
\begin{aligned}
D_{210} &= \frac{1}{3\ell\pi\omega_c\mathrm{i}}\left[-(q_0^{\mathrm{T}}F_{200})(q_0^{\mathrm{T}}F_{110}) + \frac{1}{3}|q_0^{\mathrm{T}}F_{020}|^2 + 2|q_0^{\mathrm{T}}F_{110}|^2\right], \\
D_{102} &= \frac{1}{3\ell\pi\omega_c\mathrm{i}}\left[-(q_0^{\mathrm{T}}F_{200})(q_0^{\mathrm{T}}F_{002}) + (q_0^{\mathrm{T}}F_{110})(\overline{q}_0^{\mathrm{T}}F_{002}) + 2(q_0^{\mathrm{T}}F_{002})(q_{k^*}^{\mathrm{T}}F_{101})\right],
\end{aligned}
$$

$$D_{111} = -\frac{4}{3\ell\pi\omega_c}\,\mathrm{Im}\{(q_0^{\mathrm{T}}F_{110})(q_{k^*}^{\mathrm{T}}F_{101})\},$$
$$D_{003} = -\frac{2}{3\ell\pi\omega_c}\,\mathrm{Im}\{(q_0^{\mathrm{T}}F_{002})(q_{k^*}^{\mathrm{T}}F_{101})\},$$

and

$$\begin{aligned}
E_{210} = {} & \frac{1}{3\sqrt{\ell\pi}}q_0^{\mathrm{T}}\Big[(p_{01}f_{2000}+p_{02}f_{1100})h_{0110}^{(1)}+(p_{02}f_{0200}+p_{01}f_{1100})h_{0110}^{(2)}\\
& +(\overline{p}_{01}f_{2000}+\overline{p}_{02}f_{1100})h_{0200}^{(1)}+(\overline{p}_{02}f_{0200}+\overline{p}_{01}f_{1100})h_{0200}^{(2)}\Big],\\
E_{102} = {} & \frac{1}{3\sqrt{\ell\pi}}q_0^{\mathrm{T}}\Big[(p_{01}f_{2000}+p_{02}f_{1100})h_{0002}^{(1)}+(p_{02}f_{0200}+p_{01}f_{1100})h_{0002}^{(2)}\\
& +(p_{k^*1}f_{2000}+p_{k^*2}f_{1100})h_{k^*101}^{(1)}+(p_{k^*2}f_{0200}+p_{k^*1}f_{1100})h_{k^*101}^{(2)}\Big],\\
E_{111} = {} & \frac{1}{3\sqrt{\ell\pi}}q_{k^*}^{\mathrm{T}}\Big[(p_{01}f_{2000}+p_{02}f_{1100})h_{k^*011}^{(1)}+(p_{02}f_{0200}+p_{01}f_{1100})h_{k^*011}^{(2)}\\
& +(\overline{p}_{01}f_{2000}+\overline{p}_{02}f_{1100})h_{k^*101}^{(1)}+(\overline{p}_{02}f_{0200}+\overline{p}_{01}f_{1100})h_{k^*101}^{(2)}\Big]\\
& +q_{k^*}^{\mathrm{T}}\Big[(p_{k^*1}f_{2000}+p_{k^*2}f_{1100})\Big(\frac{h_{0110}^{(1)}}{3\sqrt{\ell\pi}}+\frac{h_{(2k^*)110}^{(1)}}{3\sqrt{2\ell\pi}}\Big)\\
& \quad +(p_{k^*2}f_{0200}+p_{k^*1}f_{1100})\Big(\frac{h_{0110}^{(2)}}{3\sqrt{\ell\pi}}+\frac{h_{(2k^*)110}^{(2)}}{3\sqrt{2\ell\pi}}\Big)\Big],\\
E_{003} = {} & q_{k^*}^{\mathrm{T}}\Big[(p_{k^*1}f_{2000}+p_{k^*2}f_{1100})\Big(\frac{h_{0002}^{(1)}}{3\sqrt{\ell\pi}}+\frac{h_{(2k^*)002}^{(1)}}{3\sqrt{2\ell\pi}}\Big)\\
& +(p_{k^*2}f_{0200}+p_{k^*1}f_{1100})\Big(\frac{h_{0002}^{(2)}}{3\sqrt{\ell\pi}}+\frac{h_{(2k^*)002}^{(2)}}{3\sqrt{2\ell\pi}}\Big)\Big].
\end{aligned}$$

These formulas provide a self-contained recipe for the numerical evaluation of the normal-form coefficients; they are used in Section 5 without referring to an external appendix.

Remark 4.1. *The signs of κ_{11} and κ_{22} are intrinsic to the bifurcation and cannot be altered by any real rescaling of the amplitudes ρ and r. Therefore, in the numerical classification below, we use the normal form* (4.10) *directly rather than forcing both cubic terms to be* +1.

5. Numerical simulations

5.1. Normal-form classification

To verify the theoretical predictions near the Turing–Hopf bifurcation point, we take the parameter set

$$s = 0.44, \quad d_{11} = 3.46, \quad d_{22} = 5.58, \quad d_{12} = 0.054, \quad d_{21} = 4.08, \quad l = 5.$$

The parabolicity condition (2.3) holds since $d_{11}d_{22} - d_{12}d_{21} = 19.08648 > 0$. Solving $f(a) = 0$ in the admissible interval $(0, 1/s - 1)$ yields the Turing–Hopf point

$$a^* = 0.6790135890, \qquad c^* = 0.4390759743,$$

with critical mode $k^* = 1$ (i.e., $\mu_{k^*} = 1/25 = 0.04$). At this point, the positive equilibrium and the Hopf frequency are

$$u^* = 0.3937126754, \quad v^* = 0.5425068287, \quad \omega_c = 0.2026524743.$$

Using the coefficient formulas in Section 5, we obtain

$$\begin{aligned} \mathrm{Re}(B_{11}) &= -0.3408, \quad \mathrm{Re}(B_{21}) = 0, \\ B_{13} &= -0.2561, \qquad B_{23} = -0.2599, \\ B_{210} &= -0.0575, \qquad B_{102} = 0.0281, \\ B_{111} &= -0.1001, \qquad B_{003} = -0.1723. \end{aligned}$$

Hence, with $\mu_1 = a - a^*$ and $\mu_2 = c - c^*$, the third-order truncated normal form reads

$$\begin{cases} \dot{\rho} = -0.3408\mu_1\rho - 0.0575\rho^3 + 0.0281\rho r^2, \\ \dot{r} = -(0.2561\mu_1 + 0.2599\mu_2)r - 0.1001\rho^2 r - 0.1723r^3, \end{cases} \tag{5.1}$$

where $\rho \geq 0$ and $r \in \mathbb{R}$. Since both pure cubic coefficients are negative, the Hopf and Turing branches are supercritical.

The nontrivial equilibria of (5.1) are

$$\begin{aligned} &A_1 = (\sqrt{-5.9270\mu_1}, 0), && \mu_1 < 0, \\ &A_2^{\pm} = (0, \pm\sqrt{-1.4864\mu_1 - 1.5084\mu_2}), && \mu_2 < -0.9854\mu_1, \\ &A_3^{\pm} = (\sqrt{-5.1821\mu_1 - 0.5741\mu_2}, \pm\sqrt{1.5242\mu_1 - 1.1749\mu_2}), && \mu_2 < \min\{-9.0257\mu_1,\ 1.2974\mu_1\}, \end{aligned}$$

and the bifurcation lines in the (μ_1, μ_2)-plane are

$$\mathcal{H}_0 : \mu_1 = 0, \quad \mathcal{T} : \mu_2 = -0.9854\mu_1, \quad \mathcal{T}_1 : \mu_2 = 1.2974\mu_1, \quad \mathcal{T}_2 : \mu_2 = -9.0257\mu_1.$$

Table 1. Stability of the equilibria of the truncated normal form (5.1).

Region	Parameter range	A_0	A_1	$A_2^{\pm}$	$A_3^{\pm}$
I	$\mu_1 > 0,\ \mu_2 > -0.9854\mu_1$	Stable	Non	Non	Non
II	$\mu_1 > 0,\ -9.0257\mu_1 < \mu_2 < -0.9854\mu_1$	Unstable	Non	Stable	Non
III	$\mu_1 > 0,\ \mu_2 < -9.0257\mu_1$	Unstable	Non	Unstable	Stable
IV	$\mu_1 < 0,\ \mu_2 > -0.9854\mu_1$	Unstable	Stable	Non	Non
V	$\mu_1 < 0,\ 1.2974\mu_1 < \mu_2 < -0.9854\mu_1$	Unstable	Stable	Unstable	Non
VI	$\mu_1 < 0,\ \mu_2 < 1.2974\mu_1$	Unstable	Unstable	Unstable	Stable

These equilibria correspond to the following states of the original reaction–diffusion system: A_0 (spatially homogeneous steady state), A_1 (spatially homogeneous periodic solution), $A_2^{\pm}$ (spatially nonhomogeneous steady states), and $A_3^{\pm}$ (spatially nonhomogeneous periodic solutions). The bifurcation set is shown in Figure 1.

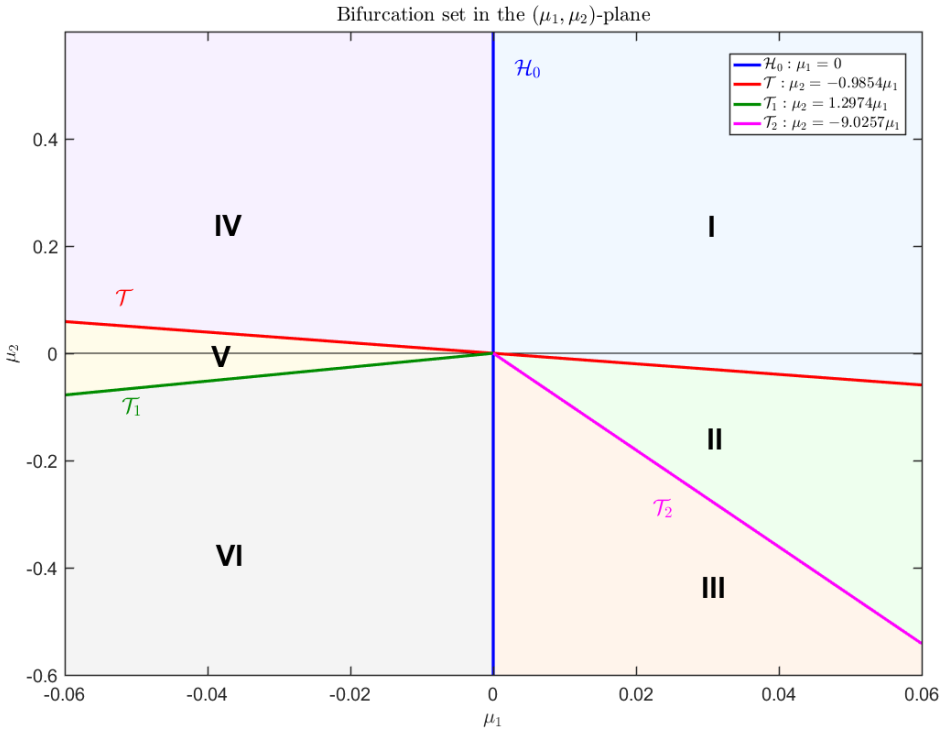

Figure 1. Bifurcation set of the truncated normal form (5.1) in the (μ_1, μ_2)-plane.

5.2. Direct numerical verification

The spatial domain $\Omega = (0, 5\pi)$ is discretized with a uniform mesh of $N_x = 181$ points, giving $\Delta x = 5\pi/180 \approx 0.0873$. The diffusion and cross-diffusion terms are treated implicitly: the discrete Laplacian with Neumann boundary conditions is inverted by a tridiagonal solver at each time step, while the reaction terms are treated explicitly. The time step $\Delta t = 0.025$ satisfies the CFL-type stability constraint dictated by the explicit reaction terms. A mesh-refinement test with $N_x = 361$ and $\Delta t = 0.0125$ produced visually identical patterns and less than 0.5 relative difference in the spatial averages, confirming that the chosen resolution is sufficient.

We simulate the full reaction–diffusion system on $\Omega = (0, 5\pi)$ with homogeneous Neumann boundary conditions. A semi-implicit finite-difference scheme is used: the diffusion and cross-diffusion terms are treated implicitly, while the reaction terms are treated explicitly. The mesh and time-stepping parameters are

$$N_x = 181, \qquad \Delta t = 0.025, \qquad T_{\max} = 1200.$$

All figures are generated by MATLAB R2016a and saved in 600 dpi PNG format.

To excite the critical Turing mode $k^* = 1$, inhomogeneous initial data are chosen along the Turing eigenvector $p_1 = (1, p_{12})^{\mathrm{T}}$ with $p_{12} \approx -0.313009$. Regions II, III, and VI possess two coexisting stable states; their two branches are selected by opposite signs of the Turing-mode perturbation.

Spatially homogeneous steady state. In Region I, the perturbation decays and the solution converges to the spatially homogeneous steady state A_0 (Figure 2).

Table 2. Parameter values and predicted stable states in the six regions.

Region	μ_1	μ_2	a	c	Predicted stable state
I	0.020	0.040	0.6990135890	0.4790759743	A_0
II	0.020	−0.025	0.6990135890	0.4140759743	$A_2^{\pm}$
III	0.015	−0.150	0.6940135890	0.2890759743	$A_3^{\pm}$
IV	−0.030	0.060	0.6490135890	0.4990759743	A_1
V	−0.005	0.0045	0.6740135890	0.4435759743	A_1
VI	−0.030	−0.080	0.6490135890	0.3590759743	$A_3^{\pm}$

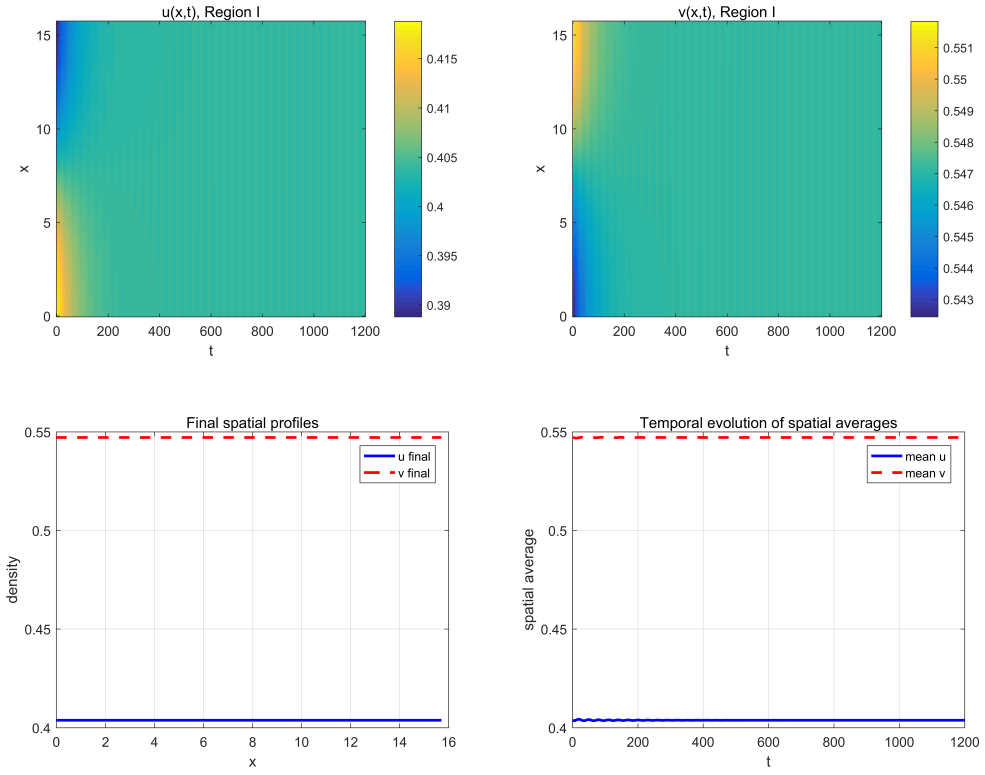

Figure 2. Region I: stable spatially homogeneous steady state. **Top left:** space-time plot of prey $u(x,t)$; **top right:** space-time plot of predator $v(x,t)$; **bottom left:** final spatial profiles of u (solid) and v (dashed); **bottom right:** temporal evolution of spatial averages. Parameters: $\mu_1 = 0.020$, $\mu_2 = 0.040$, $a = 0.6990135890$, $c = 0.4790759743$. Initial condition: $u_0 = u^* + 0.015\cos(x/5)$, $v_0 = v^* - 0.004695\cos(x/5)$.

As shown in Figure 2, the initial spatial perturbation decays rapidly and the solution settles to a flat profile. Both species maintain uniform densities across the domain, indicating that diffusion and cross-diffusion are strong enough to suppress any spatial heterogeneity when the parameters are far from the bifurcation point.

Spatially nonhomogeneous steady states. In Region II, the two opposite signs of the critical Turing-mode perturbation lead to two stable nonhomogeneous steady states A_2^+ and A_2^- (Figure 3).

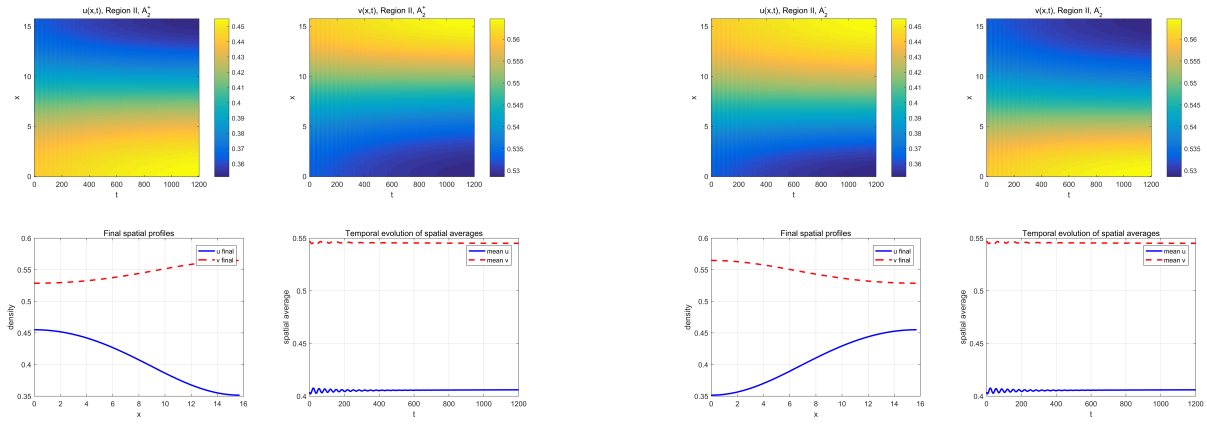

(a) A_2^+. Initial condition: $u_0 = u^* + 0.04\cos(x/5)$, $v_0 = v^* - 0.01252\cos(x/5)$.

(b) A_2^-. Initial condition: $u_0 = u^* - 0.04\cos(x/5)$, $v_0 = v^* + 0.01252\cos(x/5)$.

Figure 3. Region II: two stable spatially nonhomogeneous steady states. **Top left/right:** space-time plots of $u(x,t)$ and $v(x,t)$; **bottom left:** final spatial profiles; **bottom right:** temporal evolution of spatial averages. The two branches are mirror images selected by opposite signs of the initial Turing perturbation. Parameters: $\mu_1 = 0.020$, $\mu_2 = -0.025$, $a = 0.6990135890$, $c = 0.4140759743$.

The two panels of Figure 3 display stationary but spatially nonuniform profiles. The two branches are mirror images: in one branch, the prey density is higher near the boundaries and lower in the centre, while the predator density follows the opposite trend. This spatial segregation is induced by cross-diffusion: the predator chases the prey gradient, and the saturation in the functional response allows such a pattern to stabilize rather than oscillate. Ecologically, this means that the two species can persist in a stable, spatially segregated configuration under the same parameter values, with the final layout determined by the initial perturbation.

Spatially nonhomogeneous periodic solutions. In Regions III and VI, initial perturbations with opposite signs of the Turing mode evolve into two stable, spatially nonhomogeneous periodic solutions A_3^+ and A_3^- (Figures 4 and 5).

Figures 4 and 5 exhibit clear spatiotemporal patterns. The color bands are vertical and periodically modulated in time, indicating that the spatial profile oscillates coherently across the entire domain. The spatial averages show sustained periodic oscillations, confirming that the Hopf and Turing modes interact to produce a stable mixed mode. The two branches differ only by a spatial phase shift of π,

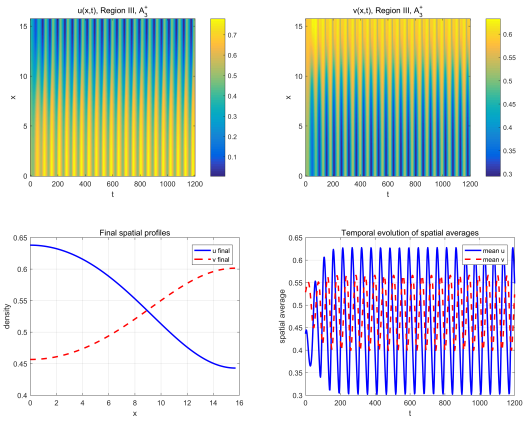

(a) A_3^+. Initial condition: $u_0 = u^* + 0.035 + 0.090\cos(x/5)$, $v_0 = v^* - 0.0175 - 0.028171\cos(x/5)$.

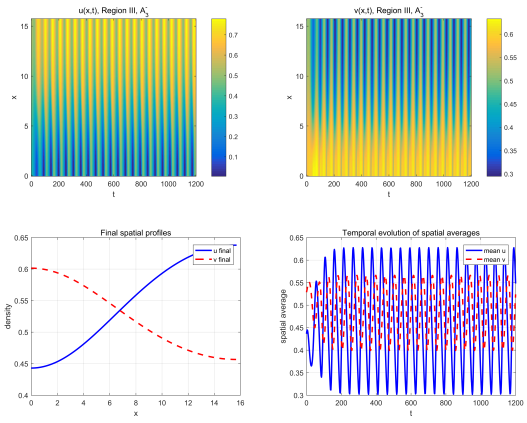

(b) A_3^-. Initial condition: $u_0 = u^* + 0.035 - 0.090\cos(x/5)$, $v_0 = v^* - 0.0175 + 0.028171\cos(x/5)$.

Figure 4. Region III: two stable, spatially nonhomogeneous periodic solutions. **Top left/right:** space-time plots of $u(x,t)$ and $v(x,t)$; **bottom left:** final spatial profiles; **bottom right:** temporal evolution of spatial averages. The vertical color bands oscillate periodically in time, indicating a mixed Turing–Hopf mode. Parameters: $\mu_1 = 0.015$, $\mu_2 = -0.150$, $a = 0.6940135890$, $c = 0.2890759743$.

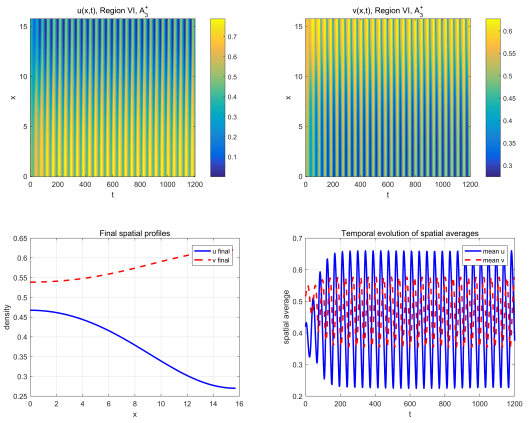

(a) A_3^+. Initial condition: $u_0 = u^* + 0.040 + 0.085\cos(x/5) + 0.025\cos(2x/5)$, $v_0 = v^* - 0.020 - 0.026606\cos(x/5) + 0.015\cos(3x/5)$.

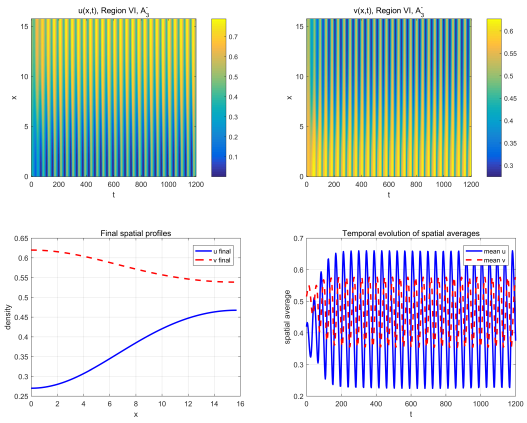

(b) A_3^-. Initial condition: $u_0 = u^* + 0.040 - 0.085\cos(x/5) + 0.025\cos(2x/5)$, $v_0 = v^* - 0.020 + 0.026606\cos(x/5) + 0.015\cos(3x/5)$.

Figure 5. Region VI: two stable, spatially nonhomogeneous periodic solutions. **Top left/right:** space-time plots of $u(x,t)$ and $v(x,t)$; **bottom left:** final spatial profiles; **bottom right:** temporal evolution of spatial averages. The two branches differ by a spatial phase shift of π. Parameters: $\mu_1 = -0.030$, $\mu_2 = -0.080$, $a = 0.6490135890$, $c = 0.3590759743$.

which corresponds to swapping the peak and trough locations of the prey and predator distributions. This type of dynamics is the hallmark of the Turing–Hopf interaction: the system exhibits both spatial structure and temporal periodicity, a phenomenon that cannot be captured by pure Turing or pure Hopf bifurcation alone.

Spatially homogeneous periodic solutions. In Regions IV and V, the solution approaches the stable, spatially homogeneous periodic solution A_1 (Figures 6 and 7).

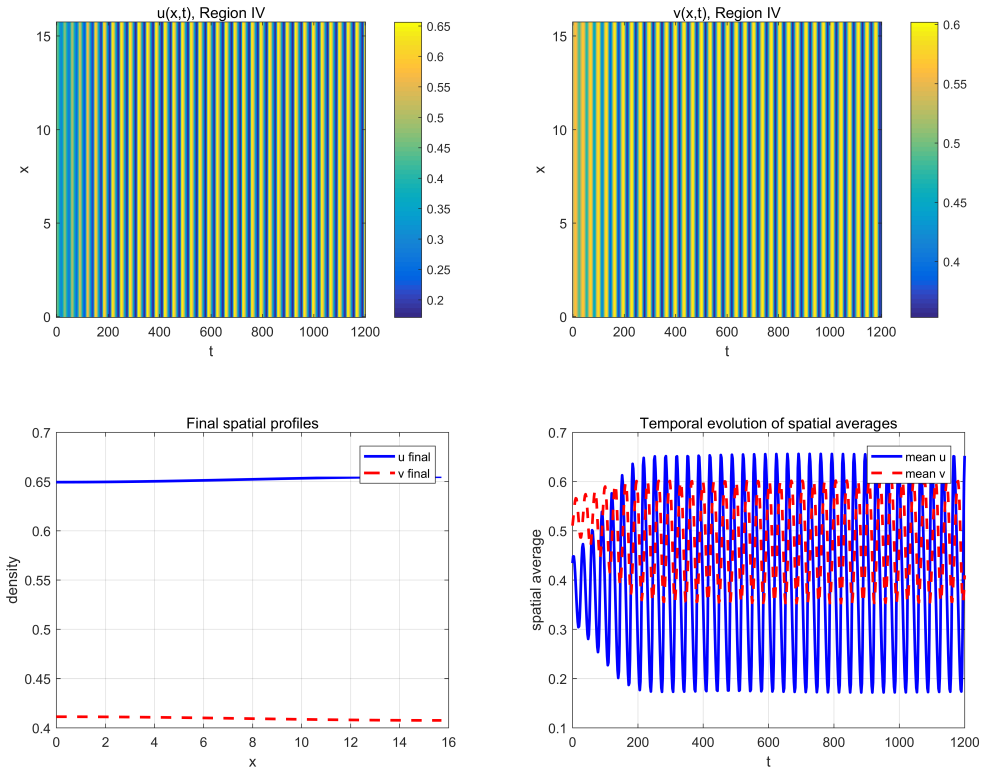

Figure 6. Region IV: stable, spatially homogeneous periodic solution. **Top left/right:** space-time plots of $u(x,t)$ and $v(x,t)$; **bottom left:** final spatial profiles; **bottom right:** temporal evolution of spatial averages. The spatial profiles are essentially flat, while the spatial averages exhibit limit-cycle oscillations. Parameters: $\mu_1 = -0.030$, $\mu_2 = 0.060$, $a = 0.6490135890$, $c = 0.4990759743$. Initial condition: $u_0 = u^* + 0.055$, $v_0 = v^* - 0.02475$.

Figures 6 and 7 show spatially uniform temporal oscillations. The final spatial profiles are essentially flat, while the spatial averages exhibit limit-cycle oscillations. This confirms that in Regions IV and V, the Turing mode is damped and only the Hopf mode survives, leading to synchronous periodic fluctuations of predator and prey densities throughout the habitat. Even though Region V lies very close to the bifurcation point, the spatially homogeneous periodic orbit remains stable against small inhomogeneous perturbations.

These simulations support the normal-form classification. In particular, changing the sign of the critical Turing-mode perturbation selects the two stable branches $A_2^{\pm}$ in Region II and $A_3^{\pm}$ in Regions III

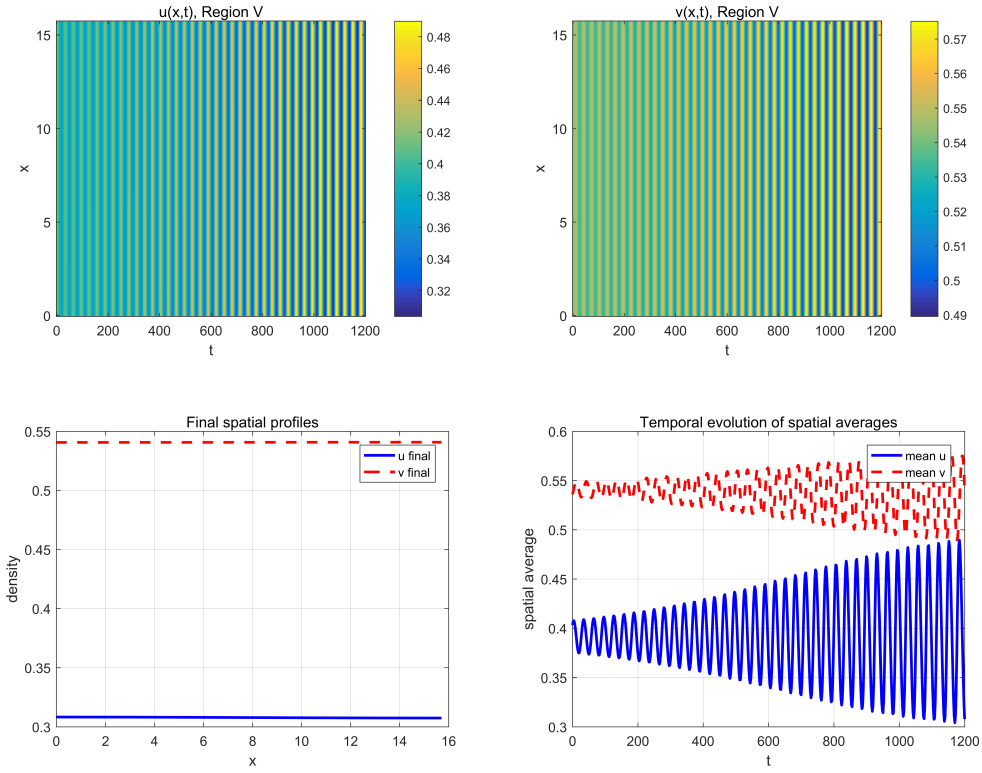

Figure 7. Region V: stable, spatially homogeneous periodic solution. **Top left/right:** space-time plots of $u(x,t)$ and $v(x,t)$; **bottom left:** final spatial profiles; **bottom right:** temporal evolution of spatial averages. Because Region V lies very close to the bifurcation point, the solution exhibits a long transient during which the oscillation amplitude grows slowly before settling into a stable limit cycle; the apparent linear growth in the early stage is therefore a transient effect, and the orbit remains spatially homogeneous and periodic for $t \gg 200$. Parameters: $\mu_1 = -0.005$, $\mu_2 = 0.0045$, $a = 0.6740135890$, $c = 0.4435759743$. Initial condition: $u_0 = u^* + 0.012 + 0.00005\cos(x/5)$, $v_0 = v^* - 0.0054 - 0.00001565\cos(x/5)$.

and VI, which is a direct consequence of the $\mathbb{Z}_2$-symmetry inherited from the cosine eigenfunction.

6. Conclusions

We have analyzed a predator–prey reaction–diffusion system with cross-diffusion and a saturated herd-type functional response. The explicit positive equilibrium and the characteristic equations for all spatial modes allowed us to derive sharp conditions for local stability, Turing instability, and the codimension-two Turing–Hopf bifurcation. Mathematically, the introduction of saturation changes the Hopf condition from a linear equation in the mortality–conversion plane to a cubic equation in the saturation parameter a, and the resulting normal-form coefficients differ quantitatively from those of the square-root model. This makes the bifurcation analysis non-perturbative in a and leads to new stability regimes that cannot be obtained by a small perturbation of the classical model. The saturation parameter a plays a decisive role: it moves the Hopf threshold from a fixed mortality value to the root of a cubic equation $f(a) = 0$, and the Turing–Hopf point is determined by the transversal intersection of the curves $a = a^*$ and $c = c_{k^*}(a)$. This structural difference distinguishes our model from the classical square-root herd model, where the bifurcation is governed by a mortality–conversion plane.

The third-order normal form on the center manifold was computed explicitly. Its coefficients were evaluated for a concrete parameter set, and the resulting truncated normal form predicts six distinct dynamical regimes near the bifurcation point. The periodic solutions emerging from the Hopf branch correspond to self-sustained population oscillations, a well-documented phenomenon in predator–prey ecology (e.g., the lynx–hare cycle). Their amplitude and frequency near the bifurcation point are determined by the normal-form coefficients κ_{11} and the Hopf frequency ω_c; because the system is autonomous, no external forcing is present and the classical forced nonlinear resonance analysis does not apply directly. Direct numerical simulations of the full reaction–diffusion system confirm these predictions and reveal four qualitatively different stable states: spatially homogeneous and inhomogeneous steady states, together with spatially homogeneous and inhomogeneous periodic solutions. The coexistence of two stable branches in Regions II, III, and VI, selected by the sign of the initial Turing perturbation, demonstrates that the system possesses multiple stable spatial configurations under the same parameter values.

From an ecological perspective, the results indicate that cross-diffusion combined with herd saturation can generate richer spatiotemporal dynamics than either mechanism alone. The saturation effect not only shifts the onset of pattern formation but also stabilizes nonuniform distributions that would otherwise collapse to homogeneous oscillations. This suggests that the geometry of prey grouping and the intensity of predator saturation are key factors in determining whether a predator–prey community settles into steady patches, periodic waves, or uniform cycles.

Several directions remain open. Extending the analysis to two-dimensional domains would allow for more complex patterns such as spots and labyrinthine structures. Incorporating time delays or stochastic forcing may further enrich the dynamics and bring the model closer to real-world ecological fluctuations. From a mathematical perspective, extending the present analysis to two-dimensional domains raises the challenge of dealing with a continuous spectrum of wave numbers and possible resonances between radial modes. Incorporating time delays would require the machinery of delay-differential equations and their center-manifold reduction, which is substantially more involved than the instantaneous diffusion case. Stochastic forcing, on the other hand, would destroy the spectral gap needed for the center-

manifold theorem and necessitate a probabilistic approach such as random dynamical systems. These extensions are therefore nontrivial but represent promising directions for future research. Finally, fitting the saturation parameter a to field data on herd-forming prey species would help assess the ecological relevance of the theoretical thresholds derived here.

Use of AI tools declaration

The authors declare they have not used Artificial Intelligence (AI) tools in the creation of this article.

Acknowledgments

This research was supported by the Northeast Forestry University College Student Innovation and Entrepreneurship Training Program Project: DCLXY-202606.

Conflict of interest

The authors declare there are no conflicts of interest.

References

1. C. S. Holling, The components of predation as revealed by a study of small-mammal predation of the European pine sawfly, *Can. Entomol.*, **91** (1959), 293–320. https://doi.org/10.4039/Ent91293-5
2. C. S. Holling, The functional response of predators to prey density and its role in mimicry and population regulation, *Mem. Entomol. Soc. Can.*, **45** (1965), 1–60. https://doi.org/10.4039/entm9745fv
3. R. Arditi, L. R. Ginzburg, Coupling in predator-prey dynamics: ratio-dependence, *J. Theor. Biol.*, **139** (1989), 311–326. https://doi.org/10.1016/S0022-5193(89)80211-5
4. J. R. Beddington, Mutual interference between parasites or predators and its effect on searching efficiency, *J. Anim. Ecol.*, **44** (1975), 331–340. https://doi.org/10.2307/3866
5. D. L. DeAngelis, R. A. Goldstein, R. V. O'Neill, A model for tropic interaction, *Ecology*, **56** (1975), 881–892. https://doi.org/10.2307/1936298
6. M. L. Rosenzweig, R. H. MacArthur, Graphical representation and stability conditions of predator-prey interactions, *Am. Nat.*, **97** (1963), 209–223. https://doi.org/10.1086/282272
7. V. Ajraldi, M. Pittavino, E. Venturino, Modeling herd behavior in population systems, *Nonlinear Anal. Real World Appl.*, **12** (2011), 2319–2338. https://doi.org/10.1016/j.nonrwa.2011.02.002
8. P. A. Braza, Predator-prey dynamics with square root functional responses, *Nonlinear Anal. Real World Appl.*, **13** (2012), 1647–1656. https://doi.org/10.1016/j.nonrwa.2011.12.014
9. X. Tang, Y. Song, Cross-diffusion induced spatiotemporal patterns in a predator-prey model with herd behavior, *Nonlinear Anal. Real World Appl.*, **24** (2015), 36–49. https://doi.org/10.1016/j.nonrwa.2014.12.006
10. A. M. Turing, The chemical basis of morphogenesis, *Philos. Trans. R. Soc. Lond. B*, **237** (1952), 37–72. https://doi.org/10.1098/rstb.1952.0012

11. J. G. Skellam, Random dispersal in theoretical populations, *Biometrika*, **38** (1951), 196–218. https://doi.org/10.1093/biomet/38.1-2.196
12. A. Okubo, S. A. Levin, *Diffusion and Ecological Problems: Modern Perspectives*, 2nd edition, Springer, New York, 2001. https://doi.org/10.1007/978-1-4757-4978-6
13. M. C. Cross, P. C. Hohenberg, Pattern formation outside of equilibrium, *Rev. Mod. Phys.*, **65** (1993), 851–1112. https://doi.org/10.1103/RevModPhys.65.851
14. S. Kondo, T. Miura, Reaction-diffusion model as a framework for understanding biological pattern formation, *Science*, **329** (2010), 1616–1620. https://doi.org/10.1126/science.1179047
15. N. Shigesada, K. Kawasaki, E. Teramoto, Spatial segregation of interacting species, *J. Theor. Biol.*, **79** (1979), 83–99. https://doi.org/10.1016/0022-5193(79)90258-3
16. Y. Lou, W. M. Ni, Diffusion, self-diffusion and cross-diffusion, *J. Differ. Equations*, **131** (1996), 79–131. https://doi.org/10.1006/jdeq.1996.0157
17. F. Yi, J. Wei, J. Shi, Bifurcation and spatiotemporal patterns in a homogeneous diffusive predator-prey system, *J. Differ. Equations*, **246** (2009), 1944–1977. https://doi.org/10.1016/j.jde.2008.10.024
18. J. Wang, J. Wei, J. Shi, Global bifurcation analysis and pattern formation in homogeneous diffusive predator-prey systems, *J. Differ. Equations*, **260** (2016), 3495–3523. https://doi.org/10.1016/j.jde.2015.10.036
19. S. Ghorai, S. Poria, Turing patterns induced by cross-diffusion in a predator-prey system in presence of habitat complexity, *Chaos Solitons Fractals*, **91** (2016), 421–429. https://doi.org/10.1016/j.chaos.2016.07.003
20. M. Banerjee, S. Ghorai, N. Mukherjee, Study of cross-diffusion induced Turing patterns in a ratio-dependent prey-predator model via amplitude equations, *Appl. Math. Model.*, **55** (2018), 383–399. https://doi.org/10.1016/j.apm.2017.11.005
21. F. Yi, Turing instability of the periodic solutions for reaction-diffusion systems with cross-diffusion and the patch model with cross-diffusion-like coupling, *J. Differ. Equations*, **281** (2021), 379–410. https://doi.org/10.1016/j.jde.2021.02.006
22. Y. Song, X. Tang, Stability, steady-state bifurcations, and Turing patterns in a predator-prey model with herd behavior and prey-taxis, *Stud. Appl. Math.*, **139** (2017), 371–404. https://doi.org/10.1111/sapm.12165
23. Y. Peng, K. Yu, Turing pattern of a diffusive predator-prey model with nonlocal delay and herd behavior, *J. Math. Anal. Appl.*, **527** (2023), 127346. https://doi.org/10.1016/j.jmaa.2023.127346
24. Y. Lv, Turing–Hopf bifurcation in the predator–prey model with cross-diffusion considering two different prey behaviours' transition, *Nonlinear Dyn.*, **107** (2022), 1357–1381. https://doi.org/10.1007/s11071-021-07058-y
25. Y. Song, T. Zhang, Y. Peng, Turing-Hopf bifurcation in the reaction-diffusion equations and its applications, *Commun. Nonlinear Sci. Numer. Simul.*, **33** (2016), 229–258. https://doi.org/10.1016/j.cnsns.2015.10.002
26. X. Tang, Y. Song, T. Zhang, Turing-Hopf bifurcation analysis of a predator-prey model with herd behavior and cross-diffusion, *Nonlinear Dyn.*, **86** (2016), 73–89. https://doi.org/10.1007/s11071-016-2873-3

27. B. D. Hassard, N. D. Kazarinoff, Y. H. Wan, *Theory and Applications of Hopf Bifurcation*, Cambridge University Press, Cambridge, 1981.

28. J. Guckenheimer, P. Holmes, *Nonlinear Oscillations, Dynamical Systems, and Bifurcations of Vector Fields*, Springer, New York, 1983. https://doi.org/10.1007/978-1-4612-1140-2

29. Y. A. Kuznetsov, *Elements of Applied Bifurcation Theory*, 3rd edtion, Springer, New York, 2004. https://doi.org/10.1007/978-1-4757-3978-7

30. T. Faria, Normal forms and Hopf bifurcation for partial differential equations with delays, *Trans. Am. Math. Soc.*, **352** (2000), 4117–4148. https://doi.org/10.1090/S0002-9947-00-02280-7

31. J. Wu, *Theory and Applications of Partial Functional-Differential Equations*, Springer, New York, 1996. https://doi.org/10.1007/978-1-4612-4050-1

AIMS Press